https://doi.org/10.1016/j.nanoen.2018.06.051

Interfacial Engineering Enables Bi@C-TiO_x Microspheres as Superpower and Long Life Anode for Lithium-ion Batteries

Zhen-Dong Huang, [a, †] Hao Lu, [a, †] Kun Qian, [b, †] Yan-Wu Fang, [a] Qing-Chuan Du, [a] Yan-Bing He, [b, *] Titus Masese, [c] Xu-Sheng Yang, [d, e] Yan-Wen Ma [a, *] and Wei Huang [a, f, *]

[a] *Key Laboratory for Organic Electronics and Information Displays & Jiangsu Key Laboratory for Biosensors, Institute of Advanced Materials (IAM), Jiangsu National Synergetic Innovation Center for Advanced Materials (SICAM), Nanjing University of Posts & Telecommunications, 9 Wenyuan Road, Nanjing, 210023, China.*

[b] *Engineering Laboratory for the Next Generation Power and Energy Storage Batteries, Graduate School at Shenzhen, Tsinghua University, Shenzhen, 518055, China.*

[c] *Research Institute of Electrochemical Energy, National Institute of Advanced Industrial Science and Technology (AIST), Ikeda, Osaka, 563-8577, Japan.*

[d] *Department of Industrial and Systems Engineering, Hong Kong Polytechnic University, Hung Hom, Kowloon, Hong Kong, China.*

[e] *Hong Kong Polytechnic University Shenzhen Research Institute, Shenzhen, 518057, China*

[f] *Institute of Flexible Electronics (SIFE), Northwestern Polytechnical University (NPU), 127 West Youyi Road, Xi'an 710072, Shaanxi, China.*

[†] Dr. Z.D. Huang, Miss H. Lu, and Mr. K. Qian contributed equally to this work.

[*]Corresponding author: Dr. Y.B. He (he.yanbing@sz.tsinghua.edu.cn), Prof. / Dr. Y.W. Ma (iamywma@njupt.edu.cn) and Prof. / Dr. W. Huang (Huangwei-huang@njtech.edu.cn).

Abstract: Bismuth (Bi), a uniquely stable pnictogen element, is deemed a promising anode material for lithium-ion batteries owing to its high volumetric capacity, moderate operating voltage and environmental friendliness. However, the application of Bi as anode is hindered by its low conductivity and large volume change during cycling. Herein, we introduce an advanced surface engineering strategy to construct Bi@C-TiO_x microspheres encapsulated by ultra-large graphene interfacial layer. Ultrafine Bi nanoparticles are confined and uniformly dispersed inside the C-TiO_x matrix, which is the pyrolysis derivative of the newly developed Bi-Ti-EG bimetal organic frameworks, with the aid of a selective graphene interfacial barrier. A three-dimensional (3D) long-range conductive network is successfully constructed by the ultra-large graphene and the carbonized derivative of Bi-Ti-EG. Additionally, the 3D carbon network and the *in-situ* formed TiO_x coupled with a porous structure act as soft buffer and hard suppressor to alleviate the huge volume change of Bi during cycling, and they also are the important electrochemically active components. Thanks to the synergistic effects intrigued by the aforementioned interfacial engineering strategy, the newly developed ultra-large graphene encapsulated Bi@C-TiO_x microspheres exhibit an exceptional superpower and outstanding cycle stability (namely, 333.3, 275 and 225 mAh g^{-1} at 1, 5 and 10 A g^{-1}, respectively, with remarkable capacity retention upon 5000 cycles), surpassing other reported Bi-based anode materials so far. This study underpins that the nanoscale surface design of electrode materials for batteries is an effective approach to significantly enhance the power capability, capacity and cyclic stability of new metal anodes.

Keywords: Bismuth; Interfacial engineering; Anode materials; Li-ion batteries; Graphene;

1. Introduction

Recently, the development of advanced energy storage materials, in particular highly safe, environmentally benign, long life, high power and high volumetric energy density anode materials for next-generation lithium ion batteries and other energy storage systems, has become one of the most important research hotspots for energy scientists globally. [1-6] Carbon materials alone cannot satisfy the future requirement of electric vehicles due to their limited gravimetric and volumetric capacity. For instance, the gravimetric and volumetric capacity of graphite anode is only 372 mAh g^{-1} and 840 mAh cm^{-3}, respectively. [7] Moreover, the remarkably low operating voltage poses severe safety issues and also causes poor rate capability resulting from the formation of dendritic lithium and thick solid-electrolyte interphase on the surface of carbon anodes. In this context, transition metals (including their oxides and sulfides (with TiO_x and $Li_4Ti_5O_{12}$ as an exception)) possess high theoretical capacity. [14, 15] In spite of their high theoretical capacity, transition metal oxides are also not promising anodes for lithium-ion batteries owing to their relatively high operating voltages (namely, 0.8 ~ 1.5 V), huge volume change, poor conductivity and slow kinetics during the conversion and (de-)alloying processes. [16-23]

Bismuth (Bi), an intriguing ancient pentavalent metal in group VA of the periodic table, has been known as a stable element with the highest atomic mass. Recently, energy scientists have also revealed layered Bi as a promising anode material for high energy density lithium-ion, sodium-ion, and potassium-ion batteries, owing to its higher volumetric capacity (3765 mAh cm^{-3}), moderate operating voltage (0.5 ~ 0.9 V vs Li^+/Li) and environmental friendliness in terms of low ecotoxicity. [6-15] The theoretical volumetric capacity of Bi is much higher than

other attractive group IVA and VA elements, including Si (2190 mAh cm^{-3}), Sn (1991 mAh cm^{-3}) and Sb (1889 mAh cm^{-3}). [11] However, Bi (as an anode) also is plagued with issues similar with other metals and their oxides, for instance, the huge volumetric and structural evolution during the charge / discharge process and a low electronic conductivity. These issues are usually responsible for the poor cyclic stability and rate capability of Bi. [6-11]

To address these issues, energy scientists have undertaken numerous strategies to alleviate the huge volume change, and also improve the conductivity of Bi nanoparticles; thus promoting fast rate capabilities and good cyclability. For example, nano-sized Bi particles embedded in carbon matrix (C/Bi composites) deliver specific capacities of 299 and 90 mAh g^{-1} at current densities of 0.1 and 2 A g^{-1}, respectively. [8] The as-prepared mesoporous Bi@C core-shell nanowires with a specific capacity of ~250 mAh g^{-1} at 1 A g^{-1} also demonstrate enhanced lithium-ion storage performance compared to that of neat Bi nanowires (~50 mAh g^{-1} at 1 A g^{-1}). [6] Equally good performance has been attained in N-doped graphene/Bi nanocomposites (~200 mAh g^{-1} at 1 A g^{-1}), [9] nano-sized Bi-embedded 1D carbon nanofibers (~230 mAh g^{-1} at 0.8 A g^{-1}), [10] and rose-like Bi@N-enriched carbon composite (~225 mAh g^{-1} at 1 A g^{-1}). [11] Nevertheless, the attained rate capabilities and cyclic stability of Bi-based composites still cannot satisfy the high energy and power requirements for future application due to the imperfect surface protection of active materials, large particle sizes and the relatively large charge transfer resistance resulting from the localized and short-range conductive networks. In view of this, it is crucial to improve the rate capability and cyclic stability (particularly at high current density) via a synergistic effect of: (1) a more effective 3D long-range (continuous) conductive network, (2) precise control of particle size and dispersivity of Bi,

and (3) the rigid suppressive effect of TiO_x phase together with the alleviating effect of soft carbon phase. Construction of a uniform and long-range stable electrical contact is one of the surefire strategies to enhance the electron transfer. [17, 18, 24] Noteworthily, a precise control of Bi nanoparticles (to below 30 nm) has also been reported as a most effective way to attain superior and reversibly electrochemical (de) alloying process. [25] In addition, a combination of a rigid suppresser together with a soft buffer has also been confirmed to effectively stabilize the structural frameworks of metal and metal oxide anode, thereby extending their cycle lifetime. [26] Taking into consideration the reported strategies, an approach that we undertook was to develop ultra-large graphene and novel Bi-Ti-bimetal organic framework which can confer the aforementioned synergistic effects. The use of Bi-Ti-bimetal organic framework as a precursor enables the *in situ* formation of ultra-fine Bi nanoparticles which are uniformly dispersed into a C-TiO_x with a well-defined morphology during the low temperature calcination process under protective or reductive atmosphere. [16] More specifically, ethylene glycol (EG) is used as a small organic molecular component to architecture dense microprism Ni-Ti-EG bimetal organic frameworks, instead of the conventional large or long chain molecules, such as 2-methylimidazole for zeolitic imidazolate frameworks.[16, 27]

Therefore, in this work, a novel Bi@C-TiO_x is developed by using a new Bi-Ti-ethylene glycol bimetal organic framework as a precursor. Ultra-large graphene oxide monolayers (with average lateral sizes of > 30 μm shown in Fig. S1), are employed to engineer the surface of Bi-Ti-ethylene glycol bimetal organic framework microsphere precursor for homogeneous encapsulation. Ultra-large graphene acts as a conductive “silk magic carpet”. During the

annealing process for preparing the ultra-large graphene encapsulated Bi@C-TiO_x microspheres, the selectively uniform ultra-large graphene interfacial barrier layer can effectively confine the ultrafine Bi nanoparticles inside the C-TiO_x matrix derived from the new Bi-Ti-EG bimetal organic framework. The obtained ultrafine Bi nanoparticles are uniformly dispersed within the C-TiO_x matrix, instead of depositing on the surface of C-TiO_x spheres. Consequently, the desired ultra-large graphene encapsulated Bi@C-TiO_x microspheres were finally obtained. Furthermore, an even and long-range (continuous) conductive 3D pathway for fast charge transfer is successfully engendered by the ultra-large graphene and amorphous carbon matrix. Benefiting from the synergistic effects derived from aforementioned interfacial and structural advantages, the as-prepared graphene encapsulated Bi@C-TiO_x microspheres anode materials exhibit ultra-long lifetimes and superpower Li-ion storage capabilities. The achieved charge capacities of graphene encapsulated Bi@C-TiO_x are 333.3, 305.4, 275 and 225 mAh g^{-1} at a current density of 1, 2.5, 5 and 10 A g^{-1}, respectively. Worthy to also note is that the charge capacity is still retained at 119.5 mAh g^{-1} even after 5000 cycles at 10 A g^{-1}.

2. Experimental

2.1. Preparation of Bi-Ti-ethylene glycol (Bi-Ti-EG) bimetal organic framework and Bi@C-TiO_x hybrid materials

The preparation process is schematically illustrated in Fig. 1. In a typical synthesis protocol, Bi-Ti-EG bimetal organic framework was prepared as a precursor using a self-templating solvothermal reaction. Stoichiometric amounts of urea, titanium butoxide and bismuth nitrate pentahydrate were first successively dissolved in a molar ratio of 3:1:1 into 60 ml of ethylene

glycol (EG) to form a clear solution under magnetic stirring at room temperature. Upon continuously stirring for 2 h, the obtained clear solution was sealed into a 100 ml teflon-lined stainless steel autoclave. To obtain the desired Bi-Ti-EG, the autoclave was thereafter put into an electro-thermal blowing dry box preheated to 160 ^{o}C. After a six-hour solvothermal reaction, Bi-Ti-EG was obtained by collecting and washing the solvothermal product with ethanol for 3 times. Subsequently, the collected Bi-Ti-EG was put in a tube furnace and calcined at temperatures ranging from 200 to 350 ^{o}C for 5 h at a heating rate of 10 ^{o}C min^{-1} in air to carbonize the organic component in Bi-Ti-EG. Finally, Bi@C-TiO$_x$ hybrid material was obtained. For clarity's sake, Bi@C-TiO$_x$ obtained upon calcination at 200, 250, 300 and 350 ^{o}C is hereafter designated as Bi@C-TiO$_x$-200, Bi@C-TiO$_x$-250, Bi@C-TiO$_x$-300 and Bi@C-TiO$_x$-350, respectively.

2.2. Preparation of ultra-large graphene oxides encapsulated Bi-Ti-EG composites and its reduced derivative

Ultra-large graphene oxide dispersion was prepared by using a modified Hummer's method. [28, 29] A typical preparation procedure of ultra-large graphene oxide generally entails four steps as follows: (1) Preparation of graphite intercalated compound by oxidizing the natural graphite flakes in the mixed acid solution of sulfuric and fuming nitric acid, (2) Rapid thermal annealing of the obtained graphite intercalated compound at 1050 ^{o}C for 15 s to obtain expanded graphite, (3) Oxygenation and expansion of expanded graphite in a mixed oxidant solution of $KMnO_4$ and sulfuric acid, and (4) Washing with diluted HCl aqueous solution and distilled water for 3 times. Upon dilution with distilled water to 400 ml, ultra-large graphene oxide dispersion (1 mg ml^{-1}) was obtained followed by a quick ultrasonication treatment.

In order to obtain the final product ultra-large graphene encapsulated Bi@C-TiO_x hybrid material, the collected Bi-Ti-EG bimetal organic framework powder was first dispersed into the as-prepared ultra-large graphene oxide dispersion with a mass ratio of 10:1. After a 5-minute ultrasonication treatment, the obtained Bi-Ti-EG/ultra-large graphene oxide dispersions were frozen apace with liquid nitrogen. Ultra-large graphene oxide encapsulated Bi-Ti-EG nanocomposites were successively obtained after freeze-drying for 36 h. Finally, the collected Bi-Ti-EG/ultra-large graphene oxide composite powders were put into a tube furnace. Following calcination in a tube furnace at 300 ^{o}C for 5 h at a heating rate of 10 ^{o}C min^{-1} under Ar atmosphere, the organic component in bimetal organic framework was decomposed concomitant with the reduction of the highly hydrogenated graphene oxide nanosheets. Finally, ultra-large graphene encapsulated Bi@C-TiO_x hybrid material was prepared successfully.

2.3. Characterization

The morphology and elemental mapping of both the as-prepared precursors and final products were characterized by using field emission scanning electron microscopy (FE-SEM, Hitachi S-4800) at an acceleration voltage of 3 kV and high-resolution transmission electron microscopy (TEM, FEI Talos) at an acceleration voltage of 100 kV. Optical photos were taken using a digital camera. Nitrogen adsorption / desorption isotherms were obtained at 77 K using an automated adsorption apparatus (Micromeritics ASAP 2020). The surface area of the samples was calculated based on the conventional Brunauer–Emmett–Teller (BET) equation. X-ray diffraction patterns of the as-prepared precursors and final products were measured on an X-ray diffractometer (Bruker D8 Advance A25) using Cu–*K*α radiation (λ = 1.54051 Å).

The diffraction patterns were recorded in a 2θ range of 10–80 ^{o} with a step size of 0.02 ^{o}. X-ray photoelectron spectroscopy (XPS, KRATOS Axis Supra) was employed to evaluate the chemical state of the samples using Al–K_{α} line as the excitation source.

To investigate the electrochemical performance of as-prepared Bi-Ti-EG bimetal organic framework, Bi@C-TiO_x and ultra-large graphene encapsulated Bi@C-TiO_x, composite electrodes were prepared by coating on copper foil a homogeneous slurry comprising a mixture of the active materials with acetylene black and polyvinylidene fluoride (in a weight ratio of active materials : acetylene black : polyvinylidene fluoride = 75 :15 :10). The electrodes were then pressed and punched out into 10 mm (in diameter) disks. Two-electrode-type Li-ion cells were assembled in an ultrapure Ar-filled glove box to investigate the Li-ion-storage performance of Bi-Ti-EG bimetal organic framework, Bi@C-TiO_x and ultra-large graphene encapsulated Bi@C-TiO_x. Note that the obtained specific capacities were calculated based on the mass loading of Bi-Ti-EG bimetal organic framework, Bi@C-TiO_x and ultra-large graphene encapsulated Bi@C-TiO_x. The electrolyte used was a 1 mol L^{-1} $LiPF_6$ in ethylene carbonate + dimethyl carbonate + ethyl methyl carbonate in a volume ratio of 1:1:1. Lithium discs were used as counter electrodes. Cyclic voltammetry (CV) was carried out in a voltage range of 0.01 to 3 V versus Li / Li^{+} at a scanning rate of 0.1 mV s^{-1}. Electrochemical impedance spectroscopy (EIS) was carried out in a frequency range of 0.01 Hz to 100 kHz, and the perturbation amplitude was set at 5 mV. Galvanostatic charge / discharge tests were performed on a battery testing system (CT2001A, Wuhan Land). Aged cells were discharged / charged within the voltage window of 0.01 to 3.0 V at current densities ranging from 0.1 to 10 A g^{-1}, respectively, under constant current mode.

3. Results and discussions

3.1. Structural morphology of Bi-Ti-EG bimetal organic framework

Sub-micron-sized spherical particles of Bi-Ti-EG bimetal organic framework were prepared by a Bi-catalyzed solvothermal reaction as illustrated in Fig. 1. Herein, EG is not only utilized as a solvent but also as both a reductive and organic complexing agent. During the solvothermal reaction process, partial Bi^{3+} are gradually reduced to elemental Bi^{0} to catalyze the growth of Bi-Ti-EG bimetal organic framework (Fig. 2a), which was confirmed by TEM and XPS analyses of Bi-Ti-EG shown in Figs. 2b-2d, and 3a. Some particles embedded in the organic matrix can be seen from the Fig. 2b and 2c. The average interplanar distance between the lattice fringes of 0.33 nm, observed in Fig. 2d, corresponds to the (012) plane of the layered phase of Bi (indexed in a rhombohedral space group of *R*-3*m* (No. 166)). [6] The deconvoluted XPS spectra of Bi 4*f* are presented in Fig. 3a. Two strong peak pairs of Bi $4f_{7/2}$ and Bi $4f_{5/2}$ for Bi-Ti-EG, located at 158.3 / 163.6 eV and centered at 156.1 / 161.4 eV can be assigned to the Bi $4f_{7/2}$ and Bi $4f_{5/2}$ of Bi^{3+} and metallic Bi^{0}, respectively. [30, 31] The energy gap between Bi $4f_{7/2}$ and Bi $4f_{5/2}$ of Bi^{3+} and Bi^{0} is around 5.3 eV, which is consistent with reported values. Additionally, the deconvoluted Ti 2*p* peaks (Fig. 3b) located at 457.6 and 459.2 eV corresponding to Ti^{3+} and Ti^{4+} in Bi-Ti-EG, respectively, indicate that more than half of the Ti^{4+} has been reduced to Ti^{3+}. [32] The deconvoluted C 1*s* and O 1*s* spectra, given in Figs. 3c and 3d, respectively, further validate the existence of C − C, C − O, Bi − O and Ti − O bonds. Based on the aforementioned XPS results, the atomic fractions of Bi 4*f*, Ti2*p*, C 1*s* and O 1*s* within Bi-Ti-EG were calculated to be 11.7%, 18.3%, 32% and 38.0%, respectively. This observation is almost consistent with the proposed structure and the growth mechanism of Bi-Ti-EG. With the existence of Bi^{3+} and elemental Bi, the dehydrogenated EG starts to react

with Ti^{4+}, $Ti^{3+}$and Bi^{3+} engulfing the Bi nanoparticles to form submicron-sized Bi-Ti-EG spheres (see Fig. 2a). The TEM micrographs, shown in Figs. 2b and 2c, manifest ~10 nm-size Bi particles that are uniformly dispersed within the Bi-Ti-EG spheres. High-resolution elemental maps further indicate a uniform distribution of Bi, Ti, O and C within the as-prepared Bi / Bi-Ti-EG submicron particles, furnished in Figs. 2e, 2f, 2g and 2h, respectively. FTIR spectra and the conspicuous sharp X-ray diffraction peaks shown in Figs. 3e and 3f further confirm the formation of Bi-Ti-EG. [33] However, we should mention here that a detailed crystal structure analysis is beyond the scope of the current study. As shown in Fig. 3e, peaks centered at 2853.5 and 2920 cm^{-1} correspond to the symmetry and anti-symmetry stretching vibration, denoted as ν_s and ν_{as}, respectively, of C–H bonding in the group of $–CH_2–$ (instead of $–CH_3$). The peaks centered at 3361, 1455, 1069 and 884 cm^{-1} can be assigned, respectively, to the ν_{OH}, δ_{OH}, ν_{CO} and γ_{OH} of C–O and O–H bonding in the group of $–CH_2–OH$. The broad peak located at 3361 cm^{-1} also arises from some certain amount of hydrate within the obtained Bi-Ti-EG, which should account for the 5.5 *wt.*% mass loss observed below 300 ^oC during the thermal analysis (shown in Fig. S2b). Based on the FTIR and XPS spectra of Bi-Ti-EG, as well as the graphite-like strong X-ray diffraction (XRD) pattern, a possible reaction mechanism between $Bi^{3+}/Ti^{3+}/Ti^{4+}$ and EG (as well as the final structure of Bi-Ti-EG) is invoked and illustrated succinctly in Figs. 1a and 1b. The metallic ions, namely $Bi^{3+}/Ti^{3+}/Ti^{4+}$, are connected by the dehydrogenated EG to form a metal-organic network shown in Fig. 1b. The metal-organic network layers interact with each other through the hydrogen bonding and intermolecular interaction to form a graphite-like layered structure. Due to the existence of hydrate and some of the partially–dehydrogenated EG ligands

connected to Ti^{4+}, the interlayer distance of the Bi-Ti-EG layer is about 0.75 nm, which is slightly smaller than the interlayer of graphene oxide (0.89 nm), [22] but much larger than graphite (0.32 nm), [27] as indicated from the XRD patterns shown in Fig. S2c. The specific surface area of Bi-Ti-EG microsphere is as high as 238.8 m^2 g^{-1}.

3.2. Synthesis of Bi-Ti-EG-derived Bi@C-TiO_x composite materials

Bi@C-TiO_x nanocomposites, namely the derivatives of Bi-Ti-EG bimetal organic framework, were prepared by annealing the Bi / Bi-Ti-EG bimetal organic framework at temperatures ranging from 200 to 350 ºC for 5 h in Ar. Upon annealing at 200 ºC, the layered-like framework is maintained without obvious morphology change. Only the interlayer spacing was slightly enlarged to some extent owing to hydrate evaporation within the Bi-Ti-EG layer (note the shift to lower diffraction angles of XRD diffraction peaks shown in Figs. 3f, S3a and S3e). When the annealing temperature is increased to 250 ºC, the Bi-Ti-EG bimetal organic framework structure starts to decompose into Bi@C-TiO_x. More layered metallic Bi quantum dots, about 10 nm, are formed and uniformly separated from the C-TiO_x matrix, due to the poor wettability between layered Bi and its matrix (as shown in Figs. 3f, S3e and S3f). The particle size of Bi nanoparticles was precisely controlled by optimizing the annealing temperature. As apparent in Fig. S3, the size of obtained Bi quantum dots increase from 10 ~ 20 nm (for Bi@C-TiO_x-250) to 30~50 nm (for Bi@C-TiO_x-300), and 60 ~ 80 nm (as for Bi@C-TiO_x-350) after heat-treatment at 250, 300 and 350 ºC for 5 h, respectively. As demonstrated in Figs. 1b, 1c and 1d, when the Bi-Ti-EG precursor was calcined at temperatures higher than the melting point of Bi nanoparticles, molten Bi flows outward (driven by the evacuating gas) and then agglomerates on the surface of C-TiO_x microspheres

forming larger particles. The XRD patterns of Bi@C-TiO_x-250, Bi@C-TiO_x-300 and Bi@C-TiO_x-350 indicate that the obtained Bi nanoparticles possess a layered structure (Fig. 3f), indexed in the space group of *R*-3*m* (No. 166), as confirmed by the high resolution SEM and TEM images shown from Figs. 4a to 4d. High resolution elemental mapping indicates that most of the Bi have separated out from the amorphous C-TiO_x matrix consisting of uniformly distributed O, Ti and C, as shown in Figs. S3i-S3l, respectively. Furthermore, the specific surface area decreases remarkably from 238.8 m^2 g^{-1} (for Bi-Ti-EG) to 93.1 m^2 g^{-1} (as for Bi@C-TiO_x-300) after annealing (see Fig. S2d).

3.3. Reduced ultra-large graphene oxide encapsulated Bi@C-TiO_x composite materials

To design a highly effective 3D conductive network, ultra-large graphene oxide (prepared by a modified Hummers' method) was used to engineer the surface of the obtained Bi-Ti-EG bimetal organic framework, namely Bi-Ti-EG/graphene oxide. As demonstrated in Fig. 1e, due to the ultra-large size (average size is larger than 30 μm.), the superior flexibility and the unique amphiphilic nature, [28, 29] Ultra-large graphene oxide was used as both a surfactant (to uniformly disperse the as-prepared Bi-Ti-EG microsphere) and an electrical clad material. Moreover, during the annealing process under Ar at 300 ºC, the ultra-large graphene can additionally act as a permselective interfacial barrier membrane. Only the evacuating gaseous water and carbon monoxide can slowly permeate through the reduced graphene oxide clad; however, the ultra-large graphene clad can effectively suppress the free movement of molten Bi, while at the same time impede the agglomeration and separation of Bi nanoparticles onto the surface of C-TiO_x, as illustrated in Figs. 1f and 1g. Figs. 4e and 4f provide an overview of the ultra-large graphene encapsulated Bi@C-TiO_x. The as-prepared Bi@C-TiO_x microspheres

are homogeneously and fully wrapped by a transparent ultra-large reduced graphene oxide (see Figs. 4e, 4f and 4g). The XRD pattern given in Fig. 3f is similar with that of neat Bi@C-TiO_x-300, which confirms the formation of ultra-large graphene encapsulated Bi@C-TiO_x. The high resolution TEM and corresponding elemental mapping images observed from Figs. 4h to 4m, confirm a uniform distribution of Bi, Ti, O and C. No conspicuously large Bi particles could be observed from the surface of microspheres. However, detachment of Bi nanoparticles from Bi@C-TiO_x-300 can be seen on the surface of graphene oxide (TEM images shown in Fig. S4), during the physical mixing of graphene oxide and Bi@C-TiO_x-300 upon ultrasonication. This observation indicates a weak binding force between the precipitated Bi nanoparticles and the C-TiO_x matrix and further underscore the importance of using graphene oxide interfacial layer during the preparation of Bi@C-TiO_x. The aforementioned results univocally support the proposed mechanism demonstrated in Figs. 1e-1g. Owing to the nature of encapsulation, the BET specific surface area of graphene encapsulated Bi@C-TiO_x further decreased to 50.3 $m^2 g^{-1}$.

3.4. The superior Li-ion storage properties

To assess the Li-ion storage properties of the developed Bi-Ti-EG, Bi@C-TiO_x-300 and ultra-large graphene encapsulated Bi@C-TiO_x, electrodes made of the target materials were used as working electrodes in Li-half cells (Further details can be found in the Experimental section). Fig. S5a shows typical voltage discharge / charge profiles during the initial cycle of the as-prepared Bi-Ti-EG, Bi@C-TiO_x-200, Bi@C-TiO_x-250 and Bi@C-TiO_x-300 at a current density of 1 A g^{-1}. It is worthy to note that the newly developed Bi-Ti-EG shows an intriguing Li-ion storage behavior. During the 1st discharge plateau located at ~1.5 V, Bi-Ti-EG converts

into metallic Bi nanoparticle and a Li-containing MOF. However, this conversion reaction is almost irreversible, taking into account the subsequent charge / discharge profiles and the cyclic voltammograms shown in Figs. 6a, 6g and 6h. The second discharge plateau located at 0.75 V (which consists mostly of metallic Bi-based anode materials), corresponds to the alloying process of Li_xBi. The reversible charge plateau centered at 0.9 V is similar to the de-alloying process of Li_xBi during the charge process of Bi-Ti-EG anode. The initial charging capacities are 461.4, 455.7, 362.7 and 354.7 mAh g^{-1} at a current density of 0.1, 0.5, 1 and 2.5 A g^{-1}, respectively. Upon (dis)charge at a current density of 0.1, 0.5, 1 and 2.5 A g^{-1} for 200 cycles, reversible capacities are still maintained 283.4, 138.2, 108.3 and 66.2 mAh g^{-1}, respectively (as shown in Fig. S5b).

Figs. S5a and S5c present the electrochemical performance of derivatives of the newly developed Bi-Ti-EG (namely Bi@C-TiO_x-200, Bi@C-TiO_x-250 and Bi@C-TiO_x-300) annealed at the temperatures of 200, 250 to 300 ^oC in Ar atmosphere. Bi@C-TiO_x-200 possesses similar Li-ion storage characteristics as Bi-Ti-EG, which does not come to a surprise considering the similarity in the crystal structure they adopt. With the decomposition of Bi-Ti-EG to form Bi@C-TiO_x, the irreversible discharging plateau located at 1.5 V disappears. As a result, the charge / discharge coulombic efficiency was significantly improved, due to the removed hydrate and the enhanced reversibility. As shown in Fig. S5c, BCT300 shows the best cyclic stability, albeit the initial specific capacity is slightly lower than Bi@C-TiO_x-250. Bi@C-TiO_x-300 maintains a capacity of 234.7 mAh g^{-1} after 200 cycles at 1 A g^{-1}, which is much higher than 151.7, 96.4 and 108.3 mAh g^{-1} obtained for Bi@C-TiO_x-250, Bi@C-TiO_x-200 and Bi-Ti-EG, respectively. In addition, the retained

capacities of Bi@C-TiO_x-300 after being (dis)charged at 0.1, 0.5, 1 and 2.5 A g^{-1} were, respectively, 449.6, 287.5, 234.7 and 167.3 mAh g^{-1} (see Fig. S5d). This performance is higher than that exhibited in Bi-Ti-EG (Fig. S5b). Akin to most metallic anode materials and other reported Bi/C nanocomposites, around 10~30 cycles are needed to not only activate the materials, but also to form a stable solid electrolyte interphase [6-11]; thus attaining relatively stable charge / discharge performance depending on the applied current density. The continuous capacity degradation during the initial several cycles presumably results from the gradual formation of solid electrolyte interphase (which in turn curtails the electrochemical activity of C, Bi, and TiO_x) and the huge volume change during the successive cycling. This is the reason as to why several cycles are required to attain relative stable performance, as shown in Figs. 5.

Upon full encapsulation by ultra-large graphene, the newly developed graphene encapsulated Bi@C-TiO_x exhibit superior Li-ion storage performance than other obtained Bi-Ti-EG and Bi@C-TiO_x-300, as presented in Fig. 5. Moreover, the discharge / charge capacities at the third cycle of graphene encapsulated Bi@C-TiO_x were 514.5 / 451.3 mAh g^{-1} at a current density of 2.5 Ag^{-1}, which is slightly higher than 475.9 / 419.7 mAh g^{-1} (obtained for Bi-Ti-EG) and 461.1 / 388.2 mAh g^{-1} (obtained for Bi@C-TiO_x-300), as can be seen in Fig. 5a. The capacity attained from the ultra-large graphene encapsulated Bi@C-TiO_x composite anode is much higher than the theoretical capacity of pure Bi. This can be attributed to the thin reduced graphene oxide layer, porous C-TiO_x and the numerous cavities encapsulated in the Bi@C-TiO_x, which provide more active sites for the storage of lithium-ion. Similar phenomenon has also been observed elsewhere. [6, 9, 11] Nevertheless, stable performance of graphene encapsulated

Bi@C-TiO_x is observed after about 20 cycles. Upon cycling at 2.5 A g^{-1} for 200 cycles, the discharge / charge capacities of graphene encapsulated Bi@C-TiO_x are still maintained at 273.5 / 272.1 mAh g^{-1}, which is much larger than of Bi@C-TiO_x-300 (170.1 / 167.3 mAh g^{-1}) and Bi-Ti-EG (66.9 / 66.2 mAh g^{-1}). This translates to a capacity of about 100 and 200 mAh g^{-1} higher than that of Bi@C-TiO_x-300 and Bi-Ti-EG, respectively, as present in Fig. 5c. The enhanced performance of graphene encapsulated Bi@C-TiO_x can be rationalized from the more uniform and smaller particle size of Bi coupled with the fully encapsulated nature of Bi@C-TiO_x, which can generate a compressive inner stress to suppress the volume change of Bi nanoparticles during the charge / discharge process, as illustrated in Fig. 6. The small drop in voltage and capacity with increase of the applied current density from 1 to 10 A g^{-1}, observed in Figs. 5b and 5d, further affirm the superior rate capability of graphene encapsulated Bi@C-TiO_x. The stable charge capacity of graphene encapsulated Bi@C-TiO_x were 333.3, 305.4, 275 and 225 mAh g^{-1} at a current density of 1, 2.5, 5 and 10 A g^{-1}, respectively. When the applied current density was reverted to 1 A g^{-1}, the recovered charge capacity was 333.6 mAh g^{-1}. Moreover, the charge capacity was maintained at 119.5 $mAhg^{-1}$ even after 5000 subsequent charge / discharge cycles at 10 A g^{-1}. The exceptional rate capability of the newly developed graphene encapsulated Bi@C-TiO_x anode materials is attributed to the judicious design of a highly effective 3D long-range (continuous) electrical conductive network by ultra-large reduced graphene oxide, as illustrated in Fig. 6c and the SEM images shown in Fig. 4. In comparison with graphene encapsulated Bi@C-TiO_x, Bi-Ti-EG is a poor conductive sub-micron-sized bimetallic metal-organic framework; thus the conductivity of Bi nanoparticles were also not satisfactory. Therefore, both Bi-Ti-EG and

Bi@C-TiO_x-300 show much higher charge transfer and contact resistance than that of graphene encapsulated Bi@C-TiO_x as illustrated in Figs. 6a and 6b, and clarified by the electrochemical impedance spectroscopy (EIS) given in Fig. 5f. The smaller voltage gap between the oxidation and reduction peaks (technically referred to as polarization) of the cyclic voltammograms shown in Figs. 5g and 5h for graphene encapsulated Bi@C-TiO_x (0.33 V), further confirm the smaller polarization derived from the smaller inner resistance than that of Bi-Ti-EG (0.47 V) and Bi@C-TiO_x-300 (0.39 V). In consideration of the above mentioned structural advantages, it is also fascinating to note that the as-prepared graphene encapsulated Bi@C-TiO_x exhibits much superior rate capability and higher capacity than many recently reported Bi-based nanostructured anode materials, such as Bi@C core-shell NWs, [6] Bi /Al_2O_3 / C, [7] Bi@C microspheres, [8] N-doped graphene / Bi, [9] Bi-embedded 1D CNFs and Bi@N-enriched carbon (see Fig. 5i). [10, 11] Therefore, the obtained performance metrics brings to the fore graphene encapsulated Bi@C-TiO_x (which is a surface-architectured Bi) as a very promising candidate anode material not only for high power lithium-ion batteries, but also sodium- and potassium-ion batteries. For instance, Wang and Lei *et al*, have indeed demonstrated that Bi bulk and porous Bi network can exhibit high capacity and ultra-long cycle-life by coupling with high performance electrolytes for both sodium-and potassium-ion batteries, respectively. [12, 13]

4. Conclusions

Ultra-large graphene encapsulated Bi@C-TiO_x was developed by an advanced surface engineering strategy. The specific capacity at at current densities of 1, 5 and 10 A g^{-1} is 333.3, 305.4, 275 and 225 mAh g^{-1}, respectively. The theoretical capacity of Bi is 385 mAh g^{-1}.

Moreover, the charge capacity is still retained at 119.5 mAh g^{-1} even after 5000 charge / discharge cycles at a high current density of 10 A g^{-1}. The superior performance of graphene-encapsulated Bi@C-TiO_x is ascribed to the unique structure (namely, a "silk-like magic carpet" encapsulation) endowed by ultra-large reduced graphene oxide. The ultra-large graphene interfacial layer can build highly effective conductive three-dimensional (3D) pathways for fast charge transfer and also generate a compressive inner stress to suppress the volume change of Bi nanoparticles during repeated (dis)charge. The surface design strategy to realize unprecedented performance of Bi proposed in this work is anticipated to pave way for the development of exotic transition metal anodes for high volumetric energy density battery chemistries.

Acknowledgments

§This work was supported by National Natural Science Foundation of China (51402155, 51701171), Priority Academic Program Development of Jiangsu Higher Education Institutions (PAPD) (YX03002), Jiangsu National Synergistic Innovation Center for Advanced Materials (SICAM), Foundation of NJUPT (NY217077), PolyU Start-up Fund for New Recruits (No. 1-ZE8R), Guangdong Province Technical Plan Project (2017B010119001 and 2017B090907005).

References

[1] H. Yin, M.-L. Cao, X.-X. Yu, H. Zhao, Y. Shen, C. Li and M.-Q. Zhu, Self-standing Bi_2O_3 nanoparticles/carbon nanofiber hybrid films as a binder-free anode for flexible sodium-ion batteries, Mater. Chem. Front., 1(2017)1615-1621.

[2] Q. H. Wang, J. T. Xu, W. C. Zhang, M. L. Mao, Z. X. Wei, L. Wang, C. Y. Cui, Y. X. Zhu, and J. M. Ma, Research progress on vanadium-based cathode materials for sodium ion batteries, J. Mater. Chem. A, 6(2018)8815-8838.

[3] M. L. Mao, C. Y. Cui, M. G. Wu, M. Zhang, T. Gao, X. L. Fan, J. Chen, T. H. Wang, J. M. Ma, C. S. Wang, Flexible ReS_2 nanosheets/N-doped carbon nanofibers-based paper as a universal anode for alkali (Li, Na, K) ion battery. Nano Energy, 45 (2018) 346–352.

[4] X. L. Deng, Z. X. Wei, C. Y. Cui, Q. H. Liu, C. Y. Wang and J. M. Ma, Oxygen-deficient anatase TiO_2@C nanospindles with pseudocapacitive contribution for enhancing lithium storage, J. Mater. Chem. A, 6(2018)4013-4022.

[5] J. J. Liang, C. C. Yuan, H. H. Li, K. Fan, Z. X. Wei, H. Q. Sun, Growth of SnO_2 Nanoflowers on N-doped Carbon Nanofibers as Anode for Li- and Na-ion Batteries Nano-Micro Lett., 10 (2018)21.

[6] R. Dai, Y. Wang, P. Da, H. Wu, M. Xu and G. Zheng, Indirect growth of mesoporous Bi@C core-shell nanowires for enhanced lithium-ion storage, Nanoscale, 6(2014)13236–13241.

[7] C.-M. Park, S. Yoon, S.-I. Lee, and H. –J. Sohn, Enhanced electrochemical properties of nanostructured bismuth-based composites for rechargeable lithium batteries, J. Power Sources, 186(2009)206–210.

[8] F. Yang, F. Yu, Z. Zhang, K. Zhang, Y. Lai, and J. Li, Bismuth nanoparticles embedded in carbon spheres as anode materials for sodium/lithium-ion batteries, Chem. Eur. J., 22(2016)2333–2338.

[9] Y. Zhang, Q. Wang, B. Wang, Y. Mei, and P. Lian, N-doped graphene/Bi nanocomposite

with excellent electrochemical properties for lithium–ion batteries, Ionics, 23(2017)1407–1415.

[10] H. Yin, Q. Li, M. Cao, W. Zhang, H. Zhao, C. Li, K. Huo, and M. Zhu, Nanosized-bismuth-embedded 1D carbon nanofibers as high-performance anodes for lithium-ion and sodium-ion batteries, Nano Res., 10(2017)2156–2167.

[11] J. –L. Lan, Y. Jin, C. Qin, Y. Yu, and X. Yang, Bio-Inspired rose-like Bi@nitrogen-enriched carbon towards high-performance lithium-ion batteries, ChemistrySelect, 2(2017)7178–7184.

[12] C. C. Wang, L. B. Wang, F. J. Li, F. Y. Cheng, and J. Chen, Bulk Bismuth as a High-Capacity and Ultralong Cycle-Life Anode for Sodium-Ion Batteries by Coupling with Glyme-Based Electrolytes, Adv. Mater. 29(2017)1702212.

[13] K. X. Lei, C. C. Wang, L. J. Liu, Y. W. Luo, C. N. Mu, F. J. Li and J. Chen, A Porous Network of Bismuth Used as Anode Material for High-Energy-Density Potassium-Ion Batteries, Angew. Chem. Int. Ed., 57(2018)4687–4691.

[14] J. He, Y.Q. Wei, T.Y. Zhai and H.Q. Li, Antimony-based materials as promising anodes for rechargeable lithium-ion and sodium-ion batteries, Mater. Chem. Front., 2(2018)437-455.

[15] S. H. Liu, H. P. Jia, L. Han, J. L. Wang, P. F. Gao, D. D. Xu, J. Yang and S. N. Che, Nanosheet-constructed porous TiO_2–B for advanced lithium ion batteries, Adv. Mater., 24(2012)3201–3204.

[16] Z.D. Huang, Z. Gong, Q. Kang, Y.W. Fang, X.S. Yang, R.Q. Liu, X.J. Lin, X.M. Feng, Y.W. Ma and D. Wang, High rate Li-ion storage properties of MOF-carbonized derivatives

coated on MnO nanowires, Mater. Chem. Front., 1(2017)1975-1981.

[17] Z. L. Xu, K. Cao, S. Abouali, M. A. Garakani, J. Q. Huang, J. Q. Huang, E. K. Heidari, H. T. Wang and J. K. Kim, Study of lithiation mechanisms of high performance carbon-coated Si anodes by in-situ microscopy, Energy Storage Mater., 3(2016)45–54.

[18] C. Miao, M. Liu, Y. B. He, X. Y. Qin, L. K. Tang, B. Huang, R. Li, B. H. Li and F. Y. Kang, Monodispersed SnO_2 nanospheres embedded in framework of graphene and porous carbon as anode for lithium ion batteries, Energy Storage Mater., 3(2016)98–105.

[19] W. Huang, X.X. Xiao, C. Engelbrekt, M.W. Zhang, S. Li, J. Ulstrup, L.J. Ci, J.K. Feng, P.C. Si and Q.J. Chi, Graphene encapsulated Fe_3O_4 nanorods assembled into a mesoporous hybrid composite used as a high-performance lithium-ion battery anode material, Mater. Chem. Front., 1(2017)1185-1193.

[20] Z. D. Huang, K. Zhang, T. T. Zhang, X. S. Yang, R. Q. Liu, Y. Li, X. J. Lin, X.M. Feng, Y. W. Ma and W. Huang, Hierarchical $NiCoO_2$ mesoporous microspheres as anode for lithium ion batteries with superior rate capability, Energy Storage Mater., 3(2016)36–44.

[21] A. A. AbdelHamid, X. Yang, J. Yang, X. Chen, and J. Y. Ying, Graphene-wrapped nickel sulfide nanoprisms with improved performance for Li-ion battery anodes and supercapacitors, Nano Energy, 26(2016)425–437.

[22] B. Chen, E. Liu, T. Cao, F. He, C. Shi, C. He, L. Ma, Q. Li, J. Li, and N. Zhao, Controllable graphene incorporation and defect engineering in MoS_2-TiO_2 based composites: Towards high-performance lithium-ion batteries anode materials, Nano Energy, 33(2017)247–256.

[23] Y. Zhou, D. Yan, H. Xu, J. Feng, X. Jiang, J. Yue, J. Yang, and Y. Qian, Hollow

nanospheres of mesoporous Co_9S_8 as a high-capacity and long-life anode for advanced lithium ion batteries, Nano Energy, 12(2015)528–537.

[24] W. Fang, N. Zhang, L. Fan, and K. Sun, Bi_2O_3 nanoparticles encapsulated by three-dimensional porous nitrogen-doped graphene for high-rate lithium ion batteries, J. Power Sources, 333(2016)30–36.

[25] L. R. Parent, Y. Cheng, P. V. Sushko, Y. Shao, J. Liu, C. –M. Wang, and N. D. Browning, Realizing the full potential of insertion anodes for Mg-ion batteries through the nanostructuring of Sn, Nano Lett., 15(2015)1177−1182.

[26] H. Wu, G. Chan, J. W. Choi, I. Ryu, Y. Yao, M. T. McDowell, S. W. Lee, A. Jackson, Y. Yang, L. Hu, and Yi Cui, Stable cycling of double-walled silicon nanotube battery anodes through solid–electrolyte interphase control, Nat. Nanotechnol., 7(2012)310–315.

[27] Z. –D. Huang, T. –T. Zhang, H. Lu, T. Masese, K. Yamamoto, R. –Q. Liu, X. –J. Lin, X. –M. Feng, X. –M. Liu, D. Wang, Y. Uchimoto, and Y. –W. Ma, Grain-boundary-rich mesoporous $NiTiO_3$ micro-prism as high tap-density, super rate and long life anode for sodium and lithium-ion batteries, Energy Storage Materials, 2017, https://doi.org/10.1016/j.ensm.2017.08.012.

[28] Z. –D. Huang, K. Zhang, T. –T. Zhang, R. –Q. Liu, X. –J. Lin, Y. Li, X. –M. Feng, Q. –B. Mei, T. Masese, Y. –W. Ma, and W. Huang, Binder-free graphene/carbon nanotube/silicon hybrid grid as freestanding anode for high capacity lithium ion batteries, Compos. Part A-Appl. S., 84(2016)386–392.

[29] Z. –D. Huang, B. Zhang, S. –W. Oh, Q. Zheng, X. Lin, A. Yousefi, and J. –K. Kim, Self-assembled reduced graphene oxide/carbon nanotube thin film as electrodes for

supercapacitors, J. Mater. Chem. , 22(2012)3591–3599.

[30] Z. Zhao, W. Zhang, Y. Sun, J. Yu, Y. Zhang, H. Wang, F. Dong, and Z. Wu, Bi cocatalyst/Bi_2MoO_6 microspheres nanohybrid with SPR-promoted visible-light photocatalysis, J. Phys. Chem. C, 120(2016)11889−11898.

[31] P. W. Wang, M. Guttag, and C. -S. Tu, Surface modification of multiferroic $BiFeO_3$ ceramic by argon sputtering, J. Surf. Eng. Mater. Adv. Technol., 4(2014)295–308.

[32] Y. Liu, Y. Shi, X. Liu, and H. Li, A facile solvothermal approach of novel Bi_2S_3/TiO_2/RGO composites with excellent visible light degradation activity for methylene blue, Appl. Surf .Sci., 396(2017)58–66.

[33] C. H. Manoratne, S. R. D. Rosa and I. R. M. Kottegoda, XRD-HTA, UV Visible, FTIR and SEM interpretation of reduced graphene oxide synthesized from high purity vein graphite, Mater. Sci. Res. India, 14(2017)19–30.

Figure captions

Fig. 1. A schematic of the proposed mechanisms for the design of Bi-Ti-ethylene glycol bimetal-organic framework (Bi-Ti-EG), Bi@C-TiO_x-300 composites derived from carbonization of Bi-Ti-EG at 300 ^oC under Ar, ultra-large graphene oxides (GO), GO-encapsulated Bi-Ti-EG composites and its reduced homologue (*viz*., graphene-encapsulated Bi@C-TiO_x).

Fig. 2. (a) SEM image, (b, c) TEM micrographs, (d) high-resolution TEM image and (e, f, g, h) the element mapping of Bi, Ti, O and C, respectively, within the Bi-Ti-EG observed in (b).

Fig. 3. The deconvoluted XPS spectra of Bi 4*f* peaks (a), Ti 2*p* peaks (b), C 1*s* peak (c), O 1*s* peak (d) and the FT-IR spectrum (e) of Bi-Ti-EG, (f) the XRD patterns (λ = 1.54051 Å) of Bi-Ti-EG, Bi@C-TiO_x-200 (BCT-1), Bi@C-TiO_x-250 (BCT-2), Bi@C-TiO_x-300 (BCT-3) and ultra-large graphene encapsulated Bi@C-TiO_x (BCT-4), respectively.

Fig. 4. (a) Low magnification and (b) high magnification SEM image, (c, d) high resolution TEM image of the as-prepared Bi@C-TiO_x-300, (e) Low, (f) medium and (g) high magnification SEM images, (h, i) TEM image of the as-prepared ultra-large graphene encapsulated Bi@C-TiO_x and (j, k, l, m) element mapping images of Bi, Ti, O and C, respectively, within the ultra-large graphene encapsulated Bi@C-TiO_x (BCT-4) observed in (i).

Fig. 5. (a) Discharge / charge voltage profiles and (c) cyclic performances of Bi-Ti-EG, Bi@C-TiO_x-300 (BCT-3) and ultra-large graphene encapsulated Bi@C-TiO_x (BCT-4) at a current density of 2.5 A g^{-1}, (b) the third cycle voltage profiles and (d) rate capability of BCT-4 at various current densities of 1, 2.5, 5, 10 A g^{-1}, respectively. (e) cyclic stability of

BCT-4 at the current density of 10 A g^{-1}, (f) electrochemical impedance spectroscopy (EIS), (g) first and (h) cyclic voltammograms (third scanning cycles) of Bi-Ti-EG, BCT-3 and BCT-4, respectively; (i) comparison on the capacity and rate performance of as-prepared ultra-large graphene encapsulated Bi@C-TiO_x with other reported Bi-based nanocomposites, including Bi@C core–shell NWs, [6] Bi/Al_2O_3/C, [7] Bi@C microspheres, [8] N-doped graphene/Bi, [9] Bi-embedded 1D CNFs and Bi@N-enriched carbon. [10, 11]

Fig. 6. Schematic illustration highlighting the various aspects endowed in the as-prepared ultra-large graphene encapsulated Bi@C-TiO_x that promote conductivity and enhance remarkable lithium-ion storage performance over the as-prepared Bi@C-TiO_x-300 and Bi-Ti-EG.

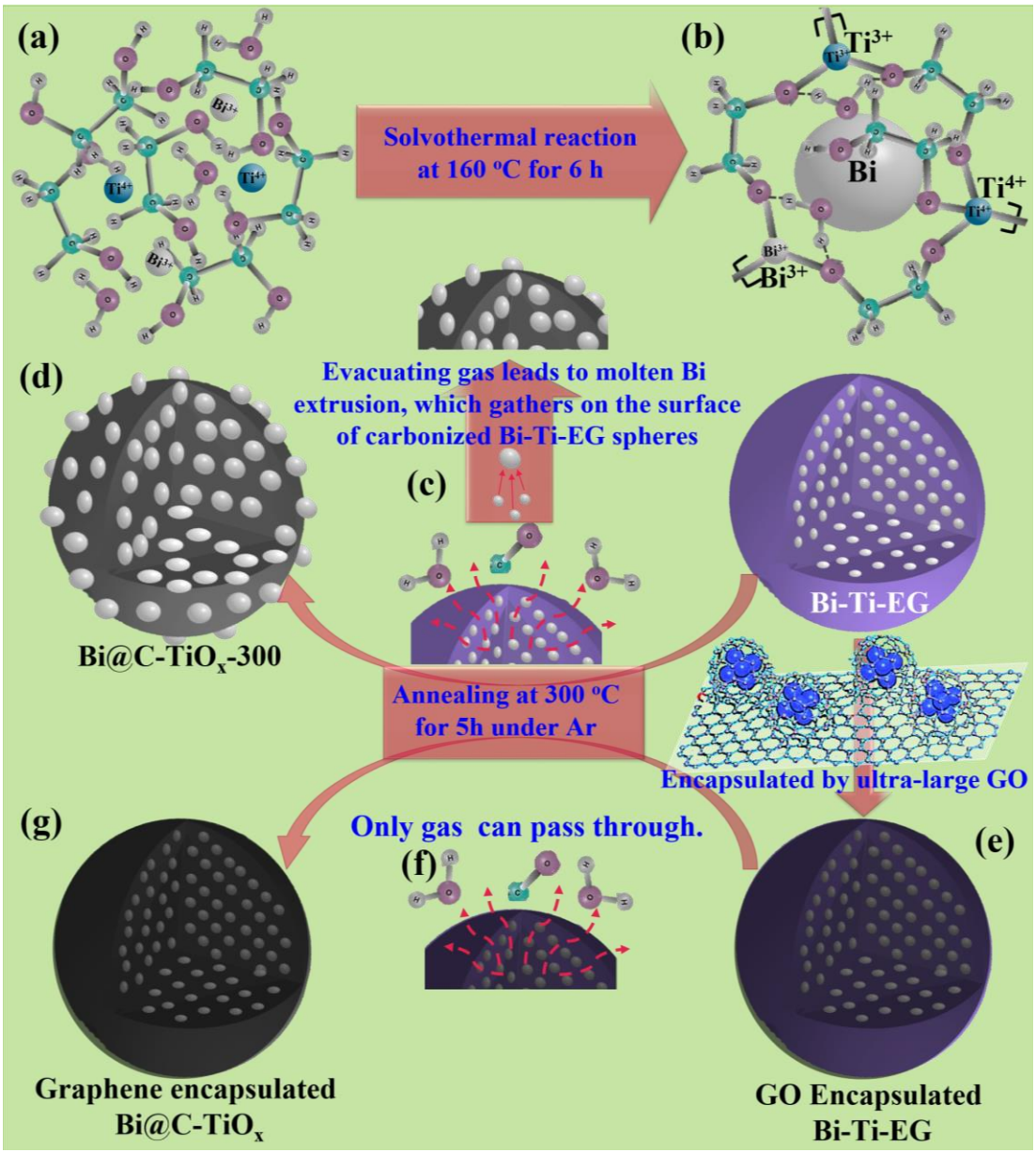

Fig. 1. A schematic of the proposed mechanisms for the design of Bi-Ti-ethylene glycol bimetal-organic framework (Bi-Ti-EG), Bi@C-TiO_x-300 composites derived from carbonization of Bi-Ti-EG at 300 °C under Ar, ultra-large graphene oxides (GO), GO-encapsulated Bi-Ti-EG composites and its reduced homologue (*viz*., graphene-encapsulated Bi@C-TiO_x).

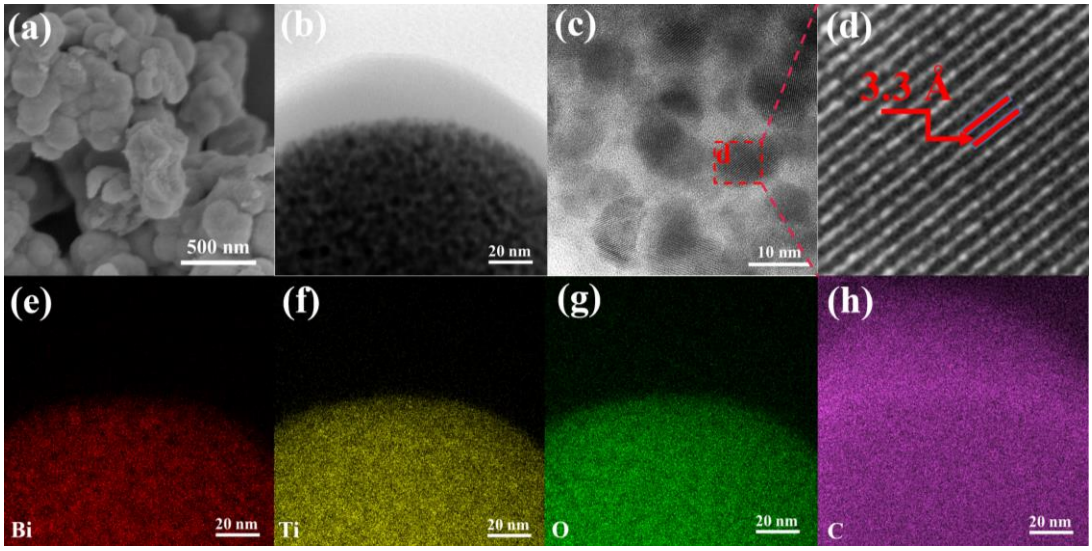

Fig. 2. (a) SEM image, (b, c) TEM micrographs, (d) high-resolution TEM image and (e, f, g, h) the element mapping of Bi, Ti, O and C, respectively, within the Bi-Ti-EG observed in (b).

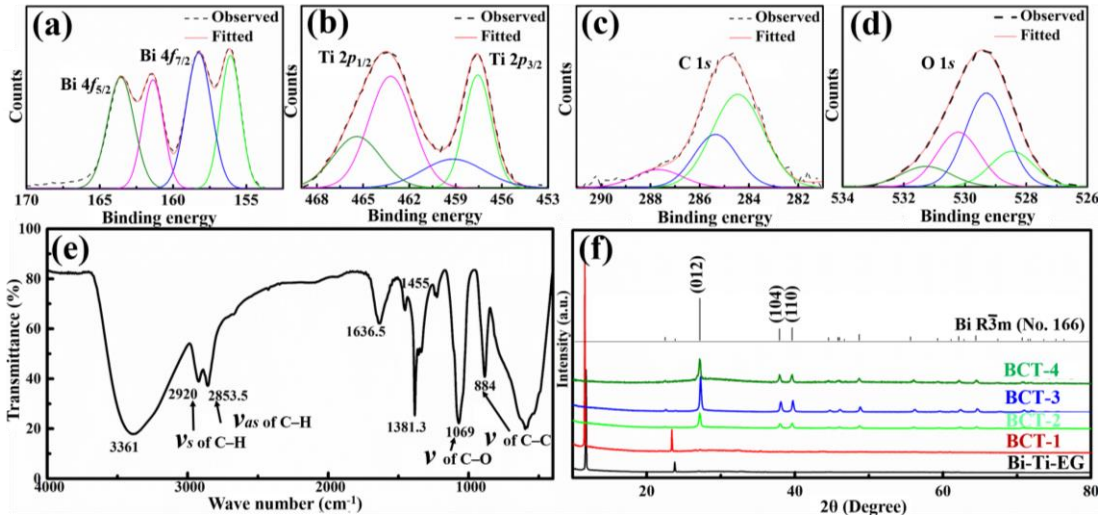

Fig. 3. The deconvoluted XPS spectra of Bi 4*f* peaks (a), Ti 2*p* peaks (b), C 1*s* peak (c), O 1*s* peak (d) and the FT-IR spectrum (e) of Bi-Ti-EG, (f) the XRD patterns (λ = 1.54051 Å) of Bi-Ti-EG, Bi@C-TiO$_x$-200 (BCT-1), Bi@C-TiO$_x$-250 (BCT-2), Bi@C-TiO$_x$-300 (BCT-3) and ultra-large graphene encapsulated Bi@C-TiO$_x$ (BCT-4), respectively.

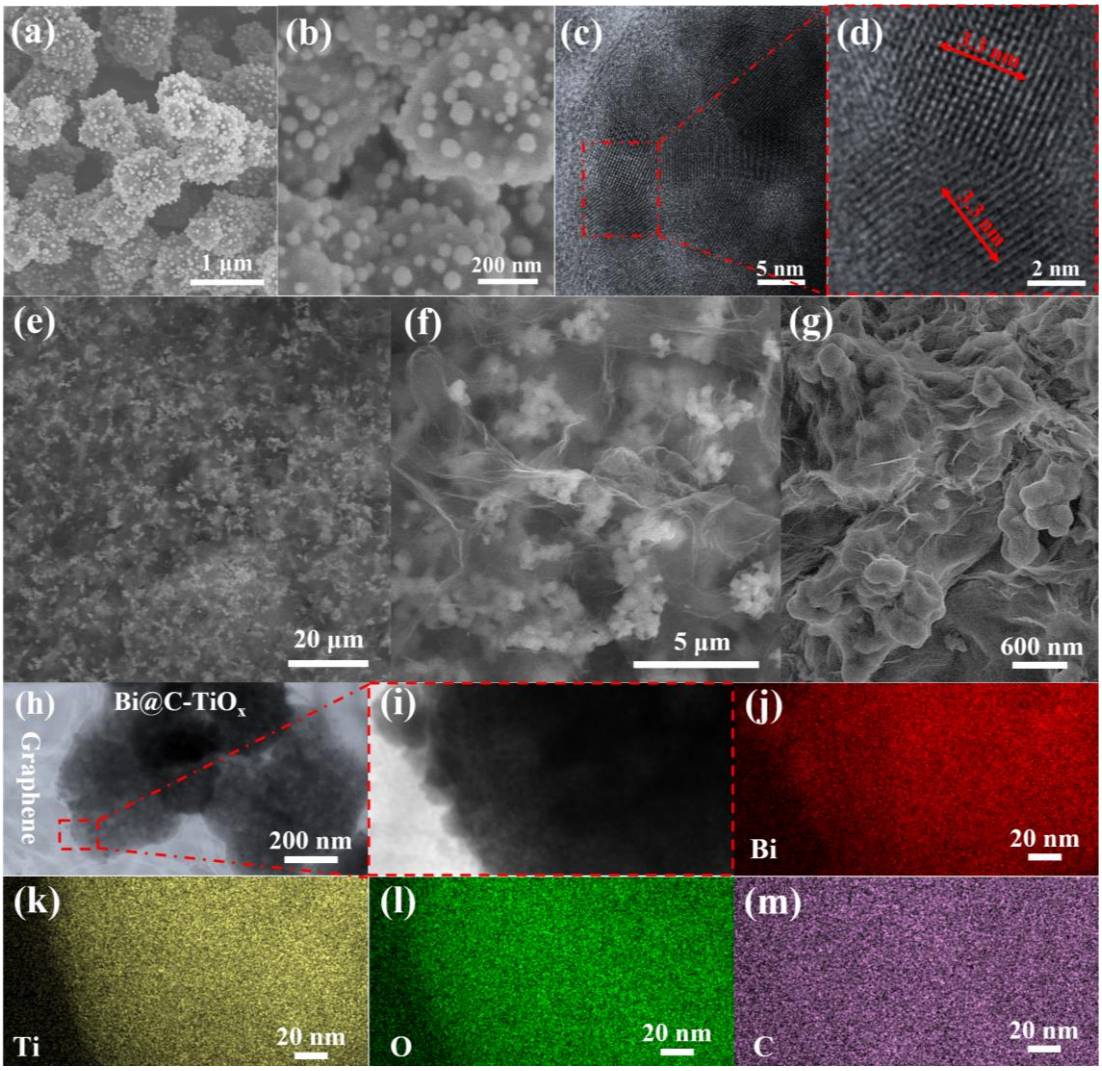

Fig. 4. (a) Low magnification and (b) high magnification SEM image, (c, d) high resolution TEM image of the as-prepared Bi@C-TiO_x-300, (e) Low, (f) medium and (g) high magnification SEM images, (h, i) TEM image of the as-prepared ultra-large graphene encapsulated Bi@C-TiO_x and (j, k, l, m) element mapping images of Bi, Ti, O and C, respectively, within the ultra-large graphene encapsulated Bi@C-TiO_x (BCT-4) observed in (i).

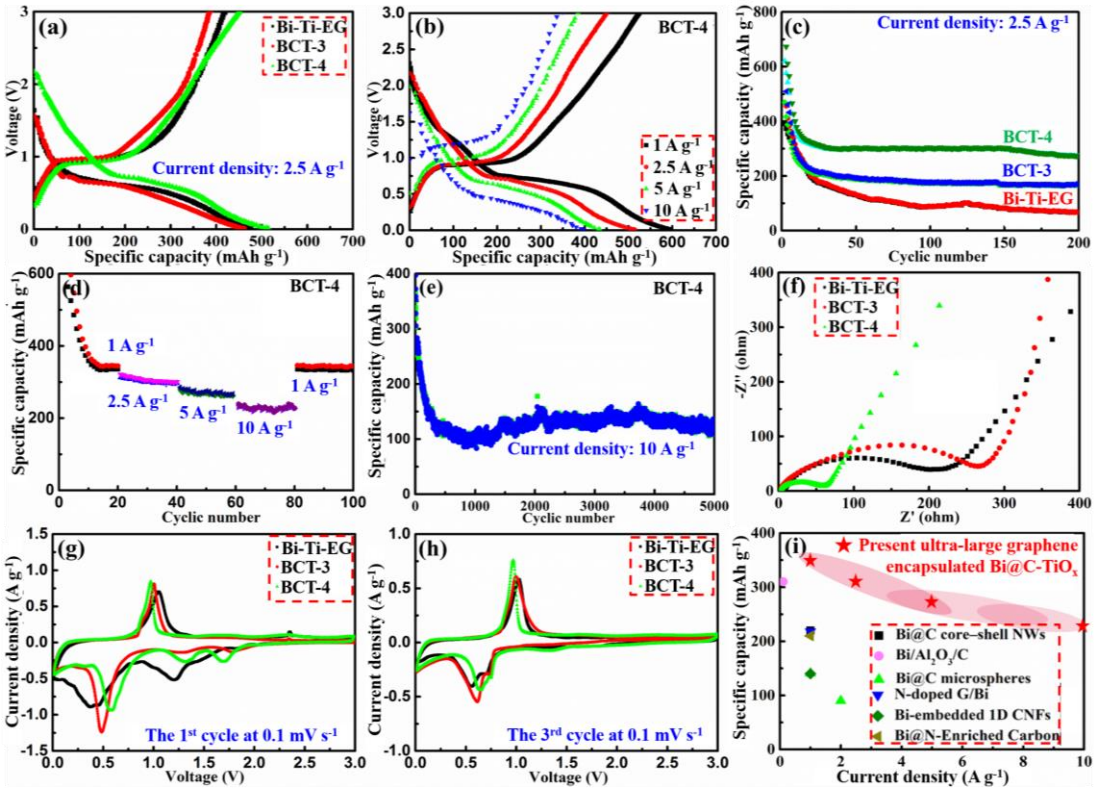

Fig. 5. (a) Discharge / charge voltage profiles and (c) cyclic performances of Bi-Ti-EG, Bi@C-TiO_x-300 (BCT-3) and ultra-large graphene encapsulated Bi@C-TiO_x (BCT-4) at a current density of 2.5 A g^{-1}, (b) the third cycle voltage profiles and (d) rate capability of BCT-4 at various current densities of 1, 2.5, 5, 10 A g^{-1}, respectively. (e) cyclic stability of BCT-4 at the current density of 10 A g^{-1}, (f) electrochemical impedance spectroscopy (EIS), (g) first and (h) cyclic voltammograms (third scanning cycles) of Bi-Ti-EG, BCT-3 and BCT-4, respectively; (i) comparison on the capacity and rate performance of as-prepared ultra-large graphene encapsulated Bi@C-TiO_x with other reported Bi-based nanocomposites, including Bi@C core–shell NWs, [6] Bi/Al_2O_3/C, [7] Bi@C microspheres, [8] N-doped graphene/Bi, [9] Bi-embedded 1D CNFs and Bi@N-enriched carbon. [10, 11]

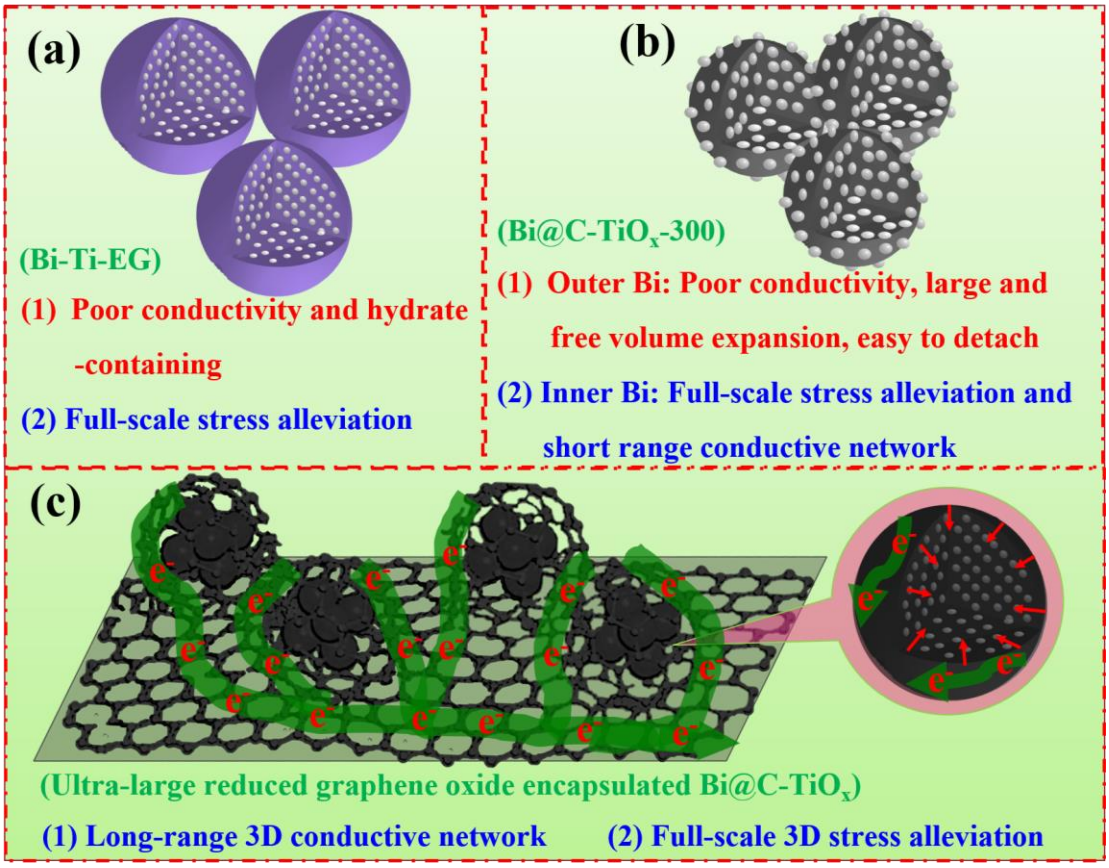

Fig. 6. Schematic illustration highlighting the various aspects endowed in the as-prepared ultra-large graphene encapsulated Bi@C-TiO_x that promote conductivity and enhance remarkable lithium-ion storage performance over the as-prepared Bi@C-TiO_x-300 and Bi-Ti-EG.

Supplementary information

Interfacial Engineering Enables Bi@C-TiO_x Microspheres as Superpower and Long Life Anode for Lithium-ion Batteries

Zhen-Dong Huang, [a, †] Hao Lu, [a, †] Kun Qian, [b, †] Yan-Wu Fang, [a] Qing-Chuan Du, [a] Yan-Bing He, [b, *] Titus Masese, [c] Xu-Sheng Yang, [d, e] Yan-Wen Ma [a, *] and Wei Huang [a, f, *]

[a] *Key Laboratory for Organic Electronics and Information Displays & Jiangsu Key Laboratory for Biosensors, Institute of Advanced Materials (IAM), Jiangsu National Synergetic Innovation Center for Advanced Materials (SICAM), Nanjing University of Posts & Telecommunications, 9 Wenyuan Road, Nanjing, 210023, China.*

[b] *Engineering Laboratory for the Next Generation Power and Energy Storage Batteries, Graduate School at Shenzhen, Tsinghua University, Shenzhen, 518055, China.*

[c] *Research Institute of Electrochemical Energy, National Institute of Advanced Industrial Science and Technology (AIST), Ikeda, Osaka, 563-8577, Japan.*

[d] *Advanced Manufacturing Technology Research Centre, Department of Industrial and Systems Engineering, The Hong Kong Polytechnic University, Hung Hom, Kowloon, Hong Kong, China.*

[e] *Hong Kong Polytechnic University Shenzhen Research Institute, Shenzhen, 518057, China*

[f] *Institute of Flexible Electronics (SIFE), Northwestern Polytechnical University (NPU), 127 West Youyi Road, Xi'an 710072, Shaanxi, China.*

[†] Dr. Z.D. Huang, Miss H. Lu, and Mr. K. Qian contributed equally to this work.

[*]Corresponding author: Dr. Y.B. He (he.yanbing@sz.tsinghua.edu.cn), Prof. / Dr. Y.W. Ma (iamywma@njupt.edu.cn) and Prof. / Dr. W. Huang (Huangwei-huang@njtech.edu.cn).

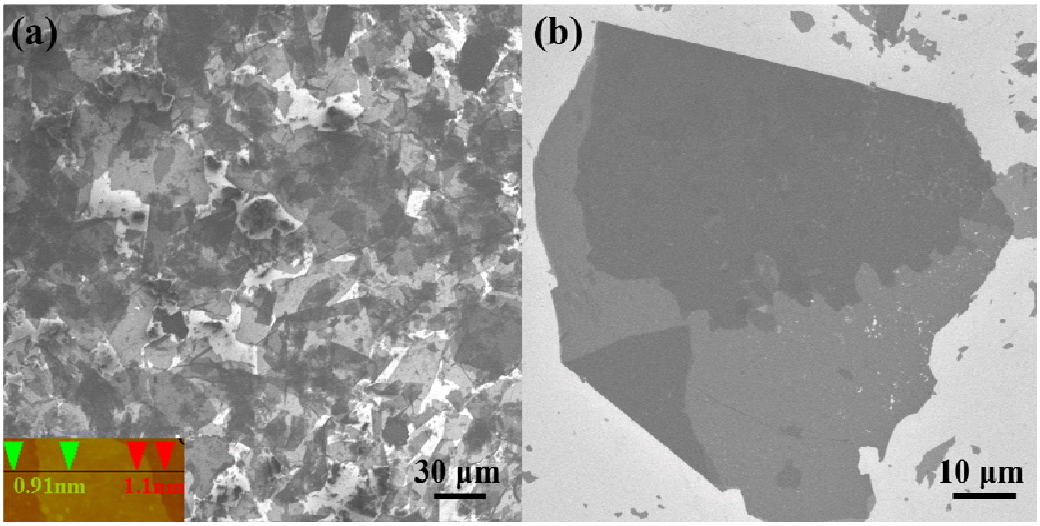

Fig. S1. Overview and typical SEM images of monolayer ultra-large graphene oxide

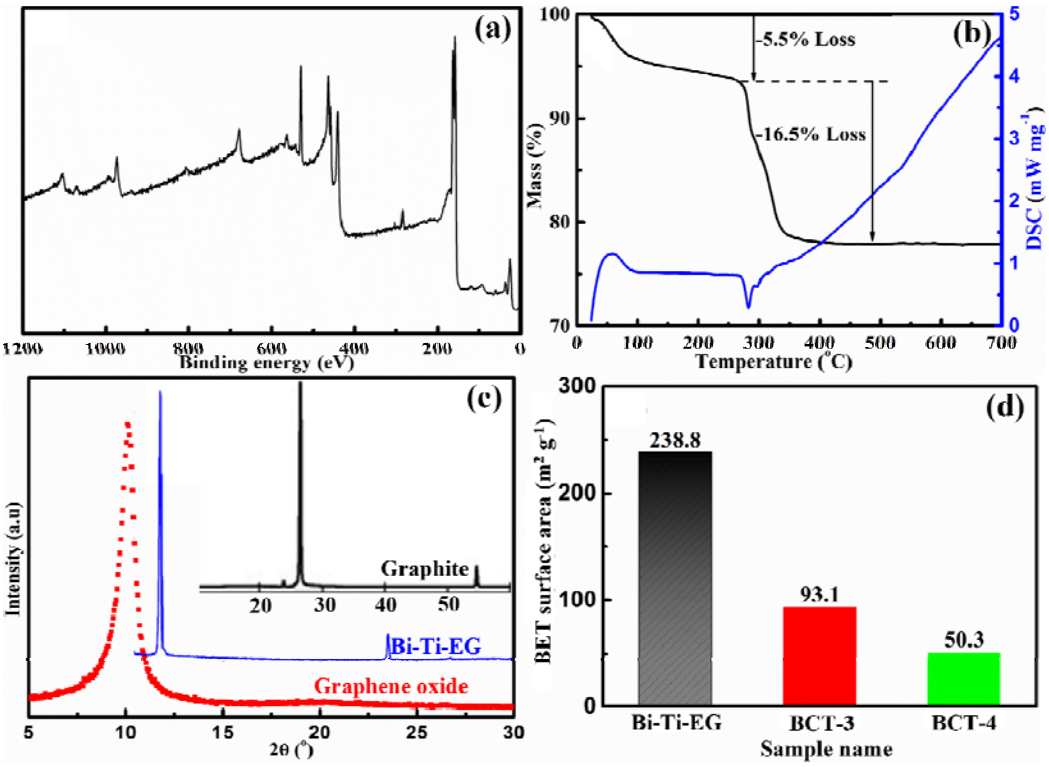

Fig. S2. (a) Full XPS spectra, (b)thermal analysis results of the as-prepared Bi-Ti-EG, (c) comparisons of the typical XRD patterns of graphene oxide, the obtained Bi-Ti-EG and commercial graphite, [22, 27] and (d) specific surface areas of the as-prepared Bi-Ti-EG, Bi@C-TiO_x-300 (BCT-3) and ultra-large reduced graphene oxide encapsulated Bi@C-TiO_x (BCT-4), respectively.

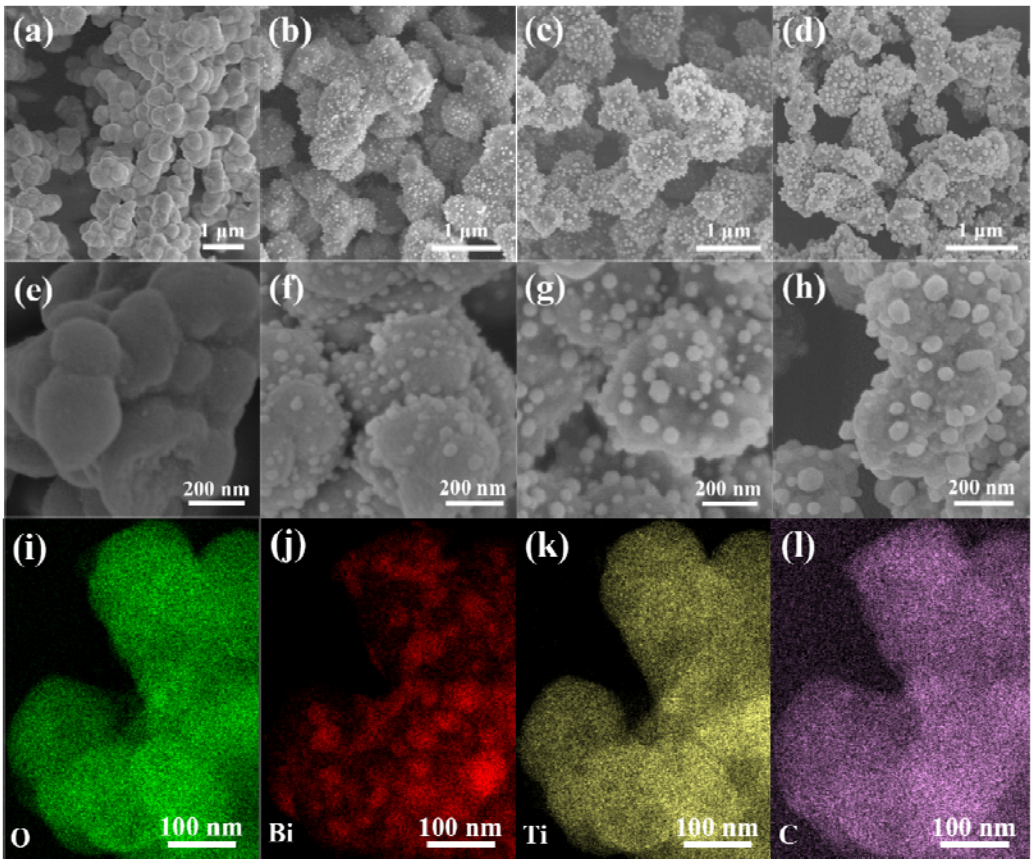

Fig. S3. Low and high magnification SEM images of Bi@C-TiO$_x$-200 (a, e), Bi@C-TiO$_x$-250 (b, f), Bi@C-TiO$_x$-300 (c, g) and Bi@C-TiO$_x$-350 (d, h), and (i, j, k and l) element mapping of O, Bi, Ti, and C, respectively, within the Bi@C-TiO$_x$-300.

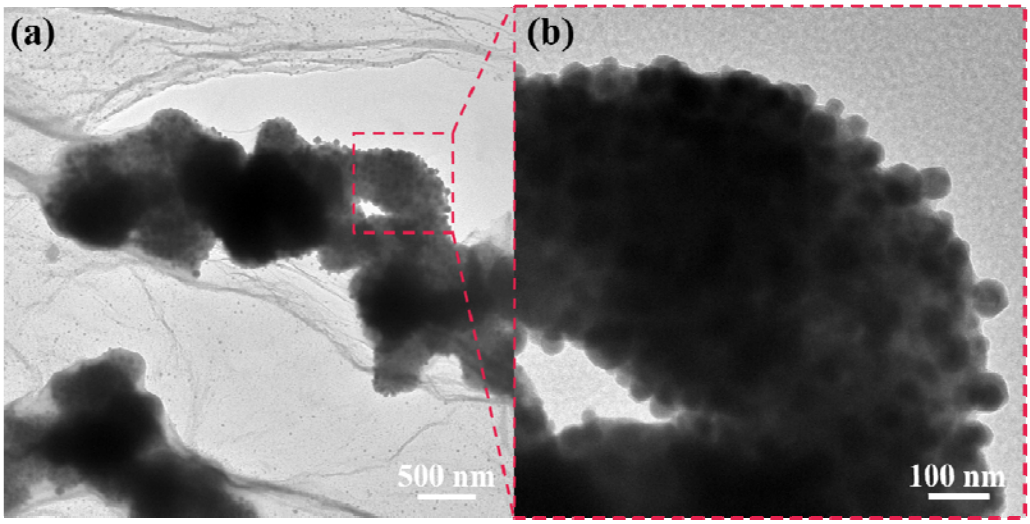

Fig. S4. TEM images of reduced graphene oxide wrapped Bi@C-TiO$_x$-300.

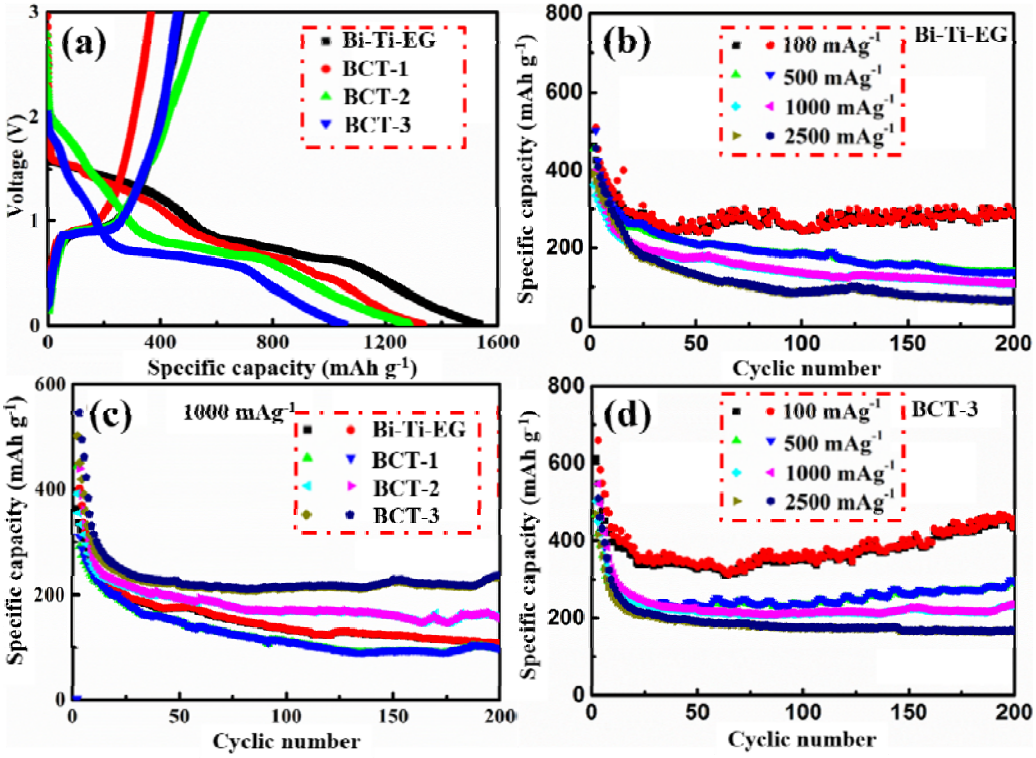

Fig. S5. (a) Initial charge / discharge voltage profiles of Bi-Ti-EG, Bi@C-TiO$_x$-200 (BCT-1), Bi@C-TiO$_x$-250 (BCT-2) and Bi@C-TiO$_x$-300 (BCT-3), (b) cyclic performance of Bi-Ti-EG at a current density of 100, 500, 1000 and 2500 mA g^{-1}, (c) cyclic performance of Bi-Ti-EG, BCT-1, BCT-2 and BCT-3 at a current density of 1000 mA g^{-1}, (d) cyclic performance of BCT-3 at a current density of 100, 500, 1000 and 2500 mA g^{-1}.